mathematics

MDPI

Article

Thermal Stress of Fractured Rock Under Solar Radiation Based on a Typical Shape Function Method

Yang Wang [1,2,3,*] and Wenhua Chen [3]

[1] China Academy of Cultural Heritage, Beijing 100029, China
[2] Technology Innovation Center for Risk Prevention and Control of Major Project Geosafety, Ministry of Natural Resources, Beijing 100083, China
[3] School of Civil Engineering, Beijing Jiaotong University, Beijing 100044, China
* Correspondence: wangyang@cach.org.cn

Abstract

Tunnel portal rocks in southern China, which are exposed to intense solar radiation and temperature fluctuations, are susceptible to thermal stress, which directly or indirectly affects the safety, stability, and normal use of a tunnel and its peripheral structures. Fractures act as conduits for solar radiation energy, converting it into thermal energy within the rock, thereby altering the thermal stress field. As formation mechanisms of rock, fractures are complex, and the nonlinear thermal conduction at fracture tips leads to thermal stress concentration. A parabolic shape function for the heat source and thermal stress at tips of rock fractures is herein proposed, and the thermal stress field of fractured rocks under solar radiation is obtained. The applicability of different fracture heat source functions for analyzing the effects of heat on rocks with varying thermodynamic properties is discussed. Compared with a linear heat source function, the thermal stress values of rock fracture tips are larger. The daily maximum $\sigma_{\theta\max}$ increases by 8.14% when $\alpha_c = 0.05$ based on the parabolic heat source function, providing more conservative results for the thermal stability analysis of fractured rock under solar radiation. Parabolic heat source functions are more reasonable for soft rocks with high thermal conductivity and low thermal deformation, while linear heat source functions are more appropriate for hard rocks. A parabolic heat source function is a typical function for analyzing the effects of heat on fractured rocks under solar radiation.

Keywords: rock mechanics; solar radiation; fractured rock; thermal stress; shape function method

MSC: 80-10; 80A05; 74A15

check for updates

Academic Editor: Smirnov Nikolay Nikolaevich

Received: 8 July 2025
Revised: 15 August 2025
Accepted: 24 August 2025
Published: 5 September 2025

Citation: Wang, Y.; Chen, W. Thermal Stress of Fractured Rock Under Solar Radiation Based on a Typical Shape Function Method. *Mathematics* **2025**, *13*, 2864. https://doi.org/10.3390/math13172864

Copyright: © 2025 by the authors. Licensee MDPI, Basel, Switzerland. This article is an open access article distributed under the terms and conditions of the Creative Commons Attribution (CC BY) license (https://creativecommons.org/licenses/by/4.0/).

1. Introduction

In high-temperature environments, the thermal stress induced by temperature fluctuations is a primary driver of rock fracture propagation [1–3]. In the southern region of China, the rocks at tunnel portals are significantly affected by high temperatures and strong solar radiation, leading to temperature fluctuations and thermal deterioration. Due to global warming, prolonged high-temperature conditions have exacerbated thermal issues in tunnel portal rocks. The temperature of exposed rocks changes synchronously and periodically with solar radiation [4–7], generating thermal stress that can induce rock failure and cracking. Aldred et al. studied the directionality of fractures in exposed rocks and concluded that solar radiation is the main cause of mechanical rock weathering [8].

The thermal stress induced by solar radiation in the surrounding rock of Longmen Grottoes ranges from 0.08 to 6.75 MPa and causes rock cracking [9,10]. Wang et al. suggested that solar radiation is the primary cause of sandstone spalling in the Danzishi cliff carvings in Chongqing [11]. Xu et al. [12] and Chen et al. [13] studied the thermal stress and thermal cracking mechanisms of large stone cultural relics such as stone tablets and rock paintings under solar radiation. Collins and Stock monitored the temperature of granite cliffs and studied the impact of solar-radiation-induced thermal stress on rock deformation [14]. Wedekind et al. demonstrated that solar radiation and thermal expansion caused tensile stress and cracking in the sandstone of the main hall of Phnom Bakheng Temple due to exposure to sunlight [15]. Amaral Vargas et al. proposed that solar radiation causes temperature changes in rocks, which leads to complex stress fields at fracture tips and results in fracture expansion and slope instability [16]. Fractures are channels of rocks that allow the transmission and transformation of solar radiation energy into rock thermal energy and are equivalent to an added source of heat in rocks, affecting rock temperature and thermal stress fields [10,17]. In the near-surface part of tunnel rocks, there are unstable tetrahedrons (key blocks) composed of intersecting fracture planes and free planes, forming sharp fractures that crack and expand easily [18,19]. This is an unstable state at the initial stage of fracture generation. With expansion of the fractures, the fracture tips become blunt due to plastic deformation caused by stress concentration and attain a certain curvature radius [20–25]. The mechanical mechanisms of fracture formation are complex, and the actual fracture shapes in rocks are often varied and irregular. Consequently, research on thermal effects on rock based on fracture heat source shape functions is crucial for the analysis of rock stability under solar radiation.

In high-temperature environments, fractured rocks at tunnel portals are highly susceptible to thermal deterioration. Although various protective measures are taken in tunnel engineering, their effectiveness remains limited due to the lack of relevant theoretical research. Fractures are important factors affecting the temperature field and thermal stress field of rocks. Fracture tips have significant physical and geometric effects and strong energy absorption capacity, which lead to thermal stress concentration. Based on the authors' previous research on the line shape function method for characterizing fracture heat sources [26], a parabolic shape function for the heat source and thermal stress at fracture tips is further proposed in this paper. The thermal stress field of fractured rocks under solar radiation is calculated, and different fracture heat source shape (triangular and parabolic) functions for analyzing thermal effects on rocks with different thermodynamic properties are proposed. Unlike previous studies that assumed linear heat source functions, this work introduces a parabolic shape function to better capture stress concentration at fracture tips, particularly in soft rocks. Compared with a linear heat source function, the thermal stress values of rock fracture tips are larger. The daily maximum $\sigma_{\theta\max}$ increases by 8.14% when $\alpha_c = 0.05$ based on a parabolic heat source function, providing more conservative results for the thermal stability analysis of fractured rock under solar radiation. The findings of this study provide a theoretical basis for evaluating thermal stability and formulating protective strategies against thermal deterioration in fractured rocks at tunnel portals in high-temperature regions of southern China.

2. Typical Function of Thermal Stress Field of Fractured Rocks Under Solar Radiation

Under the influence of solar radiation, radiation heat transfer, and convective heat transfer, the temperature fields of exposed rocks change in high-temperature environments. This leads to a non-uniform temperature distribution within the rocks, resulting in differential thermal expansion and contraction. Consequently, thermal stress is induced in rocks

due to the constraint on deformation compatibility. For rocks without fractures, the thermal stress field generated by solar radiation on the semi-infinite boundary is

$$\overline{\sigma}_{ij} = \begin{cases} -\delta_{ij}\frac{\alpha E}{1-\mu}\Delta T (i, j = x \text{ or } y) \\ 0 \quad (i \text{ or } j = z) \end{cases} \tag{1}$$

where σ_{ij} is rock thermal stress (MPa), i and j are x, y, or z, E is the rock's elastic modulus (MPa), μ is Poisson's ratio, α is rock thermal expansion coefficient (1/K), and ΔT is rock temperature difference (°C).

When there are fractures in rocks, solar radiation and atmospheric radiation enter the fractures in the form of radiant energy and are converted into rock thermal energy. There is no convective heat transfer, as the air within the fractures does not flow. A fracture is narrow and has a small opening, allowing radiant energy to be transmitted into rock through it. The energy is attenuates after being absorbed or reflected by fracture fronts and then reabsorbed and reflected multiple times within the fracture until it is completely absorbed or exits the fracture opening. The absorption rate of rock for solar shortwave radiation is 0.85–0.88, and, for atmospheric longwave radiation, it is 0.95. After multiple absorptions and reflections, the absorption rate approaches one, meaning that nearly all radiant energy entering fractures is ultimately absorbed and converted into thermal rock energy.

The formation mechanisms of fractures in rocks are complex, and the shapes of fractures are often irregular. But, during the process of radiant energy absorption and transmission into the rock by the fracture front, the temperature fields and thermal stress fields near the fracture tips are regular shapes, which can be conceptually modeled as the introduction of finite line heat sources in rocks. The geometric parameters of the fracture shape (fracture length L and fracture opening length H) affect the fracture heat source shape, as shown in Figure 1. Therefore, fracture heat source functions are established according to geometric parameters of fracture shapes, which can be used to analyze the heat transfer law between exposed fractured rocks and the external environments as well as the distribution and variation characteristics of temperature and thermal stress in fractured rocks.

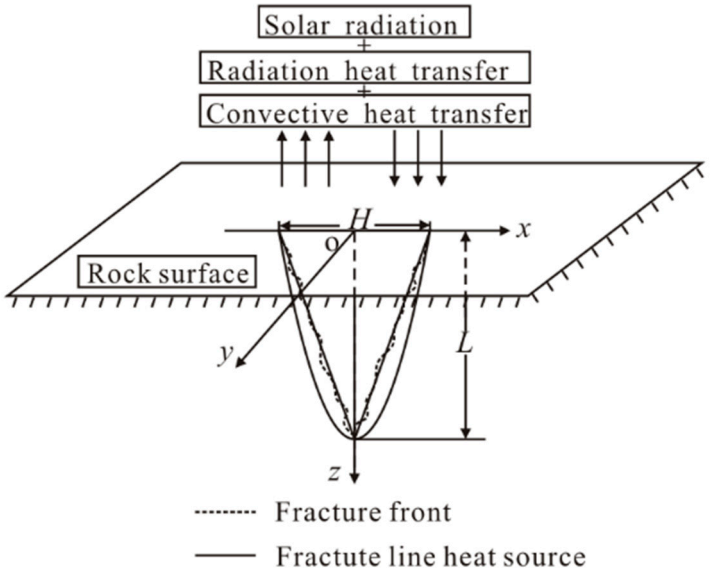


Figure 1. Heat exchange between rock and environment.

The following assumptions are adopted when establishing the fracture heat source shape function: (1) the energy density of solar radiation received by rocks is uniform;

(2) the fractures are open fractures, connected with the atmosphere, with no filling inside; (3) the fracture surface is perpendicular to the ground surface; (4) the energy density of a fracture line heat source is uniform.

The heat exchange between fractured rocks and the external environment is shown in Figure 1. For a unit instantaneous point heat source (x_0, y_0, z_0) acting at time t_0 in an infinite rock, the thermal stress field has a Green's function solution [27]:

$$\begin{aligned}\sigma_{ij}^0 = \frac{\alpha E}{4\pi\lambda R^3(1-\mu)}\Bigg\{\delta_{ij}\Bigg[\mathrm{erf}\Big(R/\sqrt{4a(t-t_0)}\Big) - \frac{R\exp\left(-R^2/4a(t-t_0)\right)}{\sqrt{\pi a(t-t_0)}} - \frac{R^3\exp\left(-R^2/4a(t-t_0)\right)}{2\sqrt{\pi}[a(t-t_0)]^{3/2}}\Bigg] \\ -\frac{(x_i-x_{i0})(x_j-x_{j0})}{R^2}\Bigg[3\mathrm{erf}\Big(R/\sqrt{4a[a(t-t_0)]}\Big) - \frac{3R\exp\left(-R^2/4a(t-t_0)\right)}{\sqrt{\pi a(t-t_0)}} - \frac{R^3\exp\left(-R^2/4a(t-t_0)\right)}{2\sqrt{\pi}[a(t-t_0)]^{3/2}}\Bigg]\Bigg\}\end{aligned} \tag{2}$$

where $a = \lambda/\rho c$ is the rock's thermal diffusivity $\left(\mathrm{m}^2/\mathrm{s}\right)$, ρ is the rock density $\left(\mathrm{kg}/\mathrm{m}^3\right)$, c is the heat capacity $(\mathrm{J}/(\mathrm{kg}\cdot\mathrm{K}))$, λ is the rock's thermal conductivity $(\mathrm{W}/(\mathrm{m}\cdot\mathrm{K}))$, t is time (s), and R is the distance from the point heat source $R = \sqrt{(x-x_0)^2 + (y-y_0)^2 + (z-z_0)^2}$.

The thermal stress field induced by a unit point heat source (x_0, y_0, z_0) during the time interval $t_{m-1} \sim t_m$ is derived as

$$\begin{aligned}\sigma_{ij}^* = \int_{t_{m-1}}^{t_m}\sigma_{ij}^0 dt_0 = \frac{\alpha E}{8\pi\lambda R(1-\mu)}\Bigg\{\delta_{ij}\Bigg[\frac{2at\mathrm{erf}\Big(R/\sqrt{4a(t_m-t_{m-1})}\Big)}{R^2} - \frac{\sqrt{4a(t_m-t_{m-1})}\exp\left(-R^2/4a(t_m-t_{m-1})\right)}{R\sqrt{\pi}} \\ -\mathrm{erfc}\left(\frac{R}{\sqrt{4a(t_m-t_{m-1})}}\right)\Bigg] - \frac{(x_i-x_{i0})(x_j-x_{j0})}{R^2}\Bigg[\frac{6a(t_m-t_{m-1})\mathrm{erf}\Big(R/\sqrt{4a(t_m-t_{m-1})}\Big)}{R^2} \\ -\frac{3\sqrt{4a(t_m-t_{m-1})}\exp\left(-R^2/4a(t_m-t_{m-1})\right)}{R\sqrt{\pi}} + \mathrm{erfc}\left(\frac{R}{\sqrt{4a(t_m-t_{m-1})}}\right)\Bigg]\Bigg\}\end{aligned} \tag{3}$$

By discretizing the solar radiation period into M hours, the heat source intensity at the m-th hour is $Q(t_m)$. The thermal stress field generated by a point heat source during the solar radiation period is

$$\sigma_{ij}^t = \sum_{m=1}^{M} Q(t_m)\sigma_{ij}^* \tag{4}$$

The thermal stress field generated by a fracture line heat source is

$$\sigma_{ij}^{tl} = \int_\Gamma \sigma_{ij}^t \mathrm{d}\Gamma \tag{5}$$

where Γ is fracture heat source. For a triangular fracture heat source, $\Gamma: z = -2Lx/H + L(0 < x < H/2)$, $z = 2Lx/H + L(-H/2 < x < 0)$; for a parabolic fracture heat source, $\Gamma: z = -4Lx^2/H + L(-H/2 < x < H/2)$, L is fracture length (m), and H is fracture opening length (m).

For a semi-infinite rock, all boundary conditions except for the shear stresses σ_{xz} and σ_{yz} at boundary can be satisfied by the mirror method, as shown in Figure 2. A mirror heat source with intensity $-Q(t)$ is placed at the symmetric position of the line heat source. For a triangular fracture heat source, $\Gamma: z = 2Lx/H - L\ (0 < x < H/2)$, $z = -2Lx/H - L\ (-H/2 < x < 0)$; for a parabolic fracture heat source, $\Gamma: z = 4Lx^2/H - L\ (-H/2 < x < H/2)$.

The thermal stress field generated by all k heat sources (line heat sources and mirror heat sources) is

$$\sigma_{1ij} = \sum_{l=1}^{k}\sigma_{ij}^{tl} \tag{6}$$

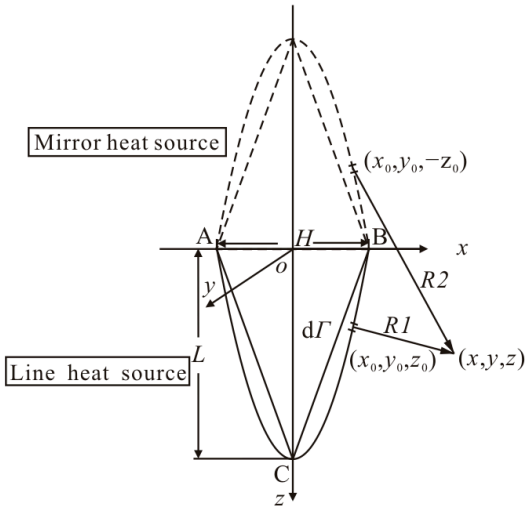


Figure 2. Heat source model.

The shear stresses (σ_{xz} and σ_{yz}) generated by line heat sources and mirror heat sources at the boundary are the same. Therefore, for semi-infinite rock, solutions to the following boundary value problem should be superimposed:

$$\begin{cases} f_x = -2\sigma_{1xz}\big|_{z=0} \\ f_y = -2\sigma_{1yz}\big|_{z=0} \end{cases} \tag{7}$$

where f_x and f_y are the sum of shear stresses generated by line heat sources and mirror heat sources at the boundary (MPa).

The stress field generated by concentrated shear stresses $f_x(\xi,\eta,0)$ and $f_y(\xi,\eta,0)$ at boundary in semi-infinite rock is

$$\sigma_{ij}^{f} = A_{ij}(x-\xi,y-\eta,z)f_x(\xi,\eta,0) + B_{ij}(x-\xi,y-\eta,z)f_y(\xi,\eta,0) \tag{8}$$

where $A_{ij}(x-\xi,y-\eta,z)$ and $B_{ij}(x-\xi,y-\eta,z)$ are stress influence coefficients:

$$\begin{gathered}
A_{xx} = \frac{x-\xi}{2\pi r^3}\left\{\frac{1-2\mu}{(r+z)^2}\left[r^2-(y-\eta)^2-\frac{2r(y-\eta)^2}{r+z}\right]-\frac{3(x-\xi)^2}{r^2}\right\} \\
A_{yy} = \frac{x-\xi}{2\pi r^3}\left\{\frac{1-2\mu}{(r+z)^2}\left[r^2-(x-\xi)^2-\frac{2r(x-\xi)^2}{r+z}\right]-\frac{3(y-\eta)^2}{r^2}\right\} \\
A_{zz} = -\frac{3(x-\xi)z^2}{2\pi r^5} \quad A_{xy} = \frac{y-\eta}{2\pi r^3}\left\{\frac{1-2\mu}{(r+z)^2}\left[-r^2+(x-\xi)^2+\frac{2r(x-\xi)^2}{r+z}\right]-\frac{3(x-\xi)^2}{r^2}\right\} \\
A_{yz} = -\frac{3(x-\xi)(y-\eta)z}{2\pi r^5} \\
A_{zx} = -\frac{3(x-\xi)^2 z}{2\pi r^5} \\
B_{xx} = \frac{y-\eta}{2\pi r^3}\left\{\frac{1-2\mu}{(r+z)^2}\left[r^2-(y-\eta)^2-\frac{2r(y-\eta)^2}{r+z}\right]-\frac{3(x-\xi)^2}{r^2}\right\} \\
B_{yy} = \frac{y-\eta}{2\pi r^3}\left\{\frac{1-2\mu}{(r+z)^2}\left[r^2-(x-\xi)^2-\frac{2r(x-\xi)^2}{r+z}\right]-\frac{3(y-\eta)^2}{r^2}\right\} \\
B_{zz} = -\frac{3(y-\eta)z^2}{2\pi r^5} \\
B_{xy} = \frac{x-\xi}{2\pi r^3}\left\{\frac{1-2\mu}{(r+z)^2}\left[-r^2+(y-\eta)^2+\frac{2r(y-\eta)^2}{r+z}\right]-\frac{3(y-\eta)^2}{r^2}\right\} \\
B_{yz} = -\frac{3(y-\eta)^2 z}{2\pi r^5} \\
B_{zx} = -\frac{3(x-\xi)(y-\eta)z}{2\pi r^5}
\end{gathered} \tag{9}$$

where r is the distance from any point in semi-infinite rock to point $(\xi, \eta, 0)$ of boundary $r = \sqrt{(x-\xi)^2 + (y-\eta)^2 + z^2}$.

As a result of integration of influence coefficients $A_{ij}(x-\xi, y-\eta, z)$ and $B_{ij}(x-\xi, y-\eta, z)$ with respect to ξ and η, $\overline{A}_{ij}(x-\xi, y-\eta, z)$, $\overline{B}_{ij}(x-\xi, y-\eta, z)$ could be obtained by

$$\begin{gathered}
\overline{A}_{xx} = -\frac{1}{2\pi}\left\{\frac{(1-2\mu)R'z^2-(z+2\mu R')(x-\xi)^2}{R'(R'+z)\left[(x-\xi)^2+z^2\right]}(y-\eta) - 2\ln(R'+y-\eta)\right\} \\
\overline{A}_{yy} = -\frac{1}{2\pi}\left[\frac{z+2\mu R'}{R'(R'+z)}(y-\eta) - 2\mu\ln(R'+y-\eta)\right] \\
\overline{A}_{zz} = \frac{(y-\eta)z^2}{2\pi R'\left[(x-\xi)^2+z^2\right]} \\
\overline{A}_{xy} = -\frac{1}{2\pi}\left[\frac{z+2\mu R'}{R'(R'+z)}(x-\xi) - 2\ln(R'+x-\xi)\right] \\
\overline{A}_{yz}(\xi,\eta) = -\frac{z}{2\pi R'} \\
\overline{A}_{zx} = -\frac{1}{2\pi}\left\{\arctan\left[\frac{(x-\xi)(y-\eta)}{R'z}\right] - \frac{(x-\xi)(y-\eta)z}{R'\left[(x-\xi)^2+z^2\right]}\right\} \\
\overline{B}_{xx} = -\frac{1}{2\pi}\left[\frac{z+2\mu R'}{R'(R'+z)}(x-\xi) - 2\mu\ln(R'+x-\xi)\right] \\
\overline{B}_{yy} = -\frac{1}{2\pi}\left\{\frac{(1-2\mu)R'z^2-(z+2\mu R')(y-\eta)^2}{R'(R'+z)\left[(y-\eta)^2+z^2\right]}(x-\xi) - 2\ln(R'+x-\xi)\right\} \\
\overline{B}_{zz} = \frac{(x-\xi)z^2}{2\pi R'\left[(y-\eta)^2+z^2\right]} \\
\overline{B}_{xy} = -\frac{1}{2\pi}\left[\frac{z+2\mu R'}{R'(R'+z)}(y-\eta) - 2\ln(R'+y-\eta)\right] \\
\overline{B}_{yz} = -\frac{1}{2\pi}\left\{\arctan\left[\frac{(x-\xi)(y-\eta)}{R'z}\right] - \frac{(x-\xi)(y-\eta)z}{R'\left[(y-\eta)^2+z^2\right]}\right\} \\
\overline{B}_{zx} = -\frac{z}{2\pi R'}
\end{gathered} \tag{10}$$

By discretizing the boundary into S rectangular elements and assuming shear stress on each element uniform, the stress field in semi-infinite rock generated by shear stress on the boundary could be obtained by

$$\sigma_{2ij} = \sum_{s=1}^{S}\left[\overline{A}_{ij}f_{sx} + \overline{B}_{ij}f_{sy}\right]\Big|_{\xi_{s1}}^{\xi_{s2}}\Big|_{\eta_{s1}}^{\eta_{s2}} \tag{11}$$

where s is the s-th element, f_{sx} and f_{sy} are the values of f_x and f_y at center of the s-th element, ξ_{s1} and ξ_{s2} are region restrictions of the s-th rectangular element in the x direction, η_{s1} and η_{s2} are region restrictions of the s-th rectangular element in the y direction.

The thermal stress generated by the fracture heat source under solar radiation is

$$\overline{\overline{\sigma}}_{ij} = \sigma_{1ij} + \sigma_{2ij} \tag{12}$$

Combining Equations (1) and (12), the typical function for the thermal stress field of fractured rocks under solar radiation is

$$\sigma_{ij} = \overline{\sigma}_{ij} + \overline{\overline{\sigma}}_{ij} \tag{13}$$

To validate the analytical model, finite element simulations were also conducted under identical boundary conditions.

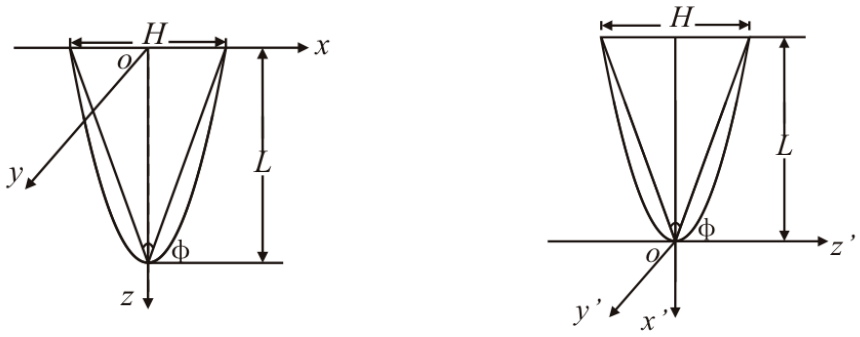
A brittle crack in a rock satisfies maximum tensile stress theory, and the stress intensity factor of a surface fracture is

$$\begin{cases} K_{\mathrm{I}} = \kappa\sigma_y\sqrt{L\pi} \\ K_{\mathrm{II}} = \sigma_{yz}\sqrt{L\pi} \end{cases} \tag{14}$$

where K_{I} and K_{II} are the stress intensity factors of fractures, κ is the correction coefficient of the surface fracture stress intensity factor.

A local coordinate system is established with the fracture tip point as the origin. The direction perpendicular to a fracture is in the y' direction, the direction of fracture extension is in the z' direction, and the direction perpendicular to the $y'z'$ plane is in the x' direction, as shown in Figure 3. The coordinate could be transformed as

$$\begin{cases} x' = z - L \\ y' = y \\ z' = x \end{cases} \tag{15}$$



(**a**) Original coordinate (**b**) Shifted coordinate

Figure 3. The change in the coordinate system.

The circumferential tensile stress near a fracture tip is

$$\sigma_\theta = \frac{1}{2\sqrt{2\pi r}} \cos\frac{\theta}{2}[K_{\mathrm{I}}(1+\cos\theta) - 3K_{\mathrm{II}}\sin\theta] \tag{16}$$

where r and θ are the polar radius and polar angle in coordinate system $ox'y'$, respectively; $x' = r\cos\theta$; $y' = r\sin\theta$.

When σ_θ reaches the maximum value, fracture initiation angle θ_c satisfies

$$\begin{cases} \partial\sigma_\theta/\partial\theta' = 0 \\ \partial^2\sigma_\theta/\partial\theta'^2 \le 0 \end{cases} \tag{17}$$

The maximum circumferential tensile stress is

$$\sigma_{\theta\max} = \frac{1}{\sqrt{2\pi r_c}} \cos\frac{\theta_c}{2}\left(K_{\mathrm{I}}\cos^2\frac{\theta_c}{2} - \frac{3}{2}K_{\mathrm{II}}\sin\theta_c\right) \tag{18}$$

where r_c is critical dimension of the maximum circumferential tensile stress (m).

When the maximum circumferential tensile stress exceeds the tensile strength of a rock $\sigma_{\theta\max} \ge [\sigma_m]$, a fracture will expand.

3. Thermal Stress Field of Rocks Based on Typical Fracture Heat Source Functions

Using fractured granite from the tunnel portals of the Guangzhou–Shenzhen–Hong Kong High-Speed Railway as a case study, the thermal stress of fractured rocks under solar radiation is calculated based on typical fracture heat source shape (triangular or parabolic) functions, and the influence of different heat source functions on the thermal

stress values of fractured rocks is analyzed. The relevant environmental conditions and granite properties are summarized in Figure 4 and Table 1 [28].

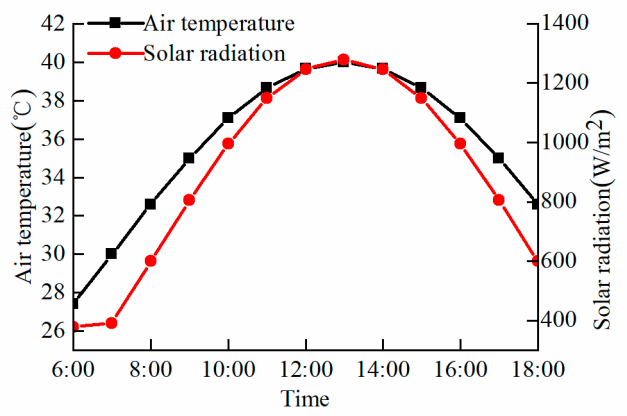


Figure 4. Air temperature and solar radiation.

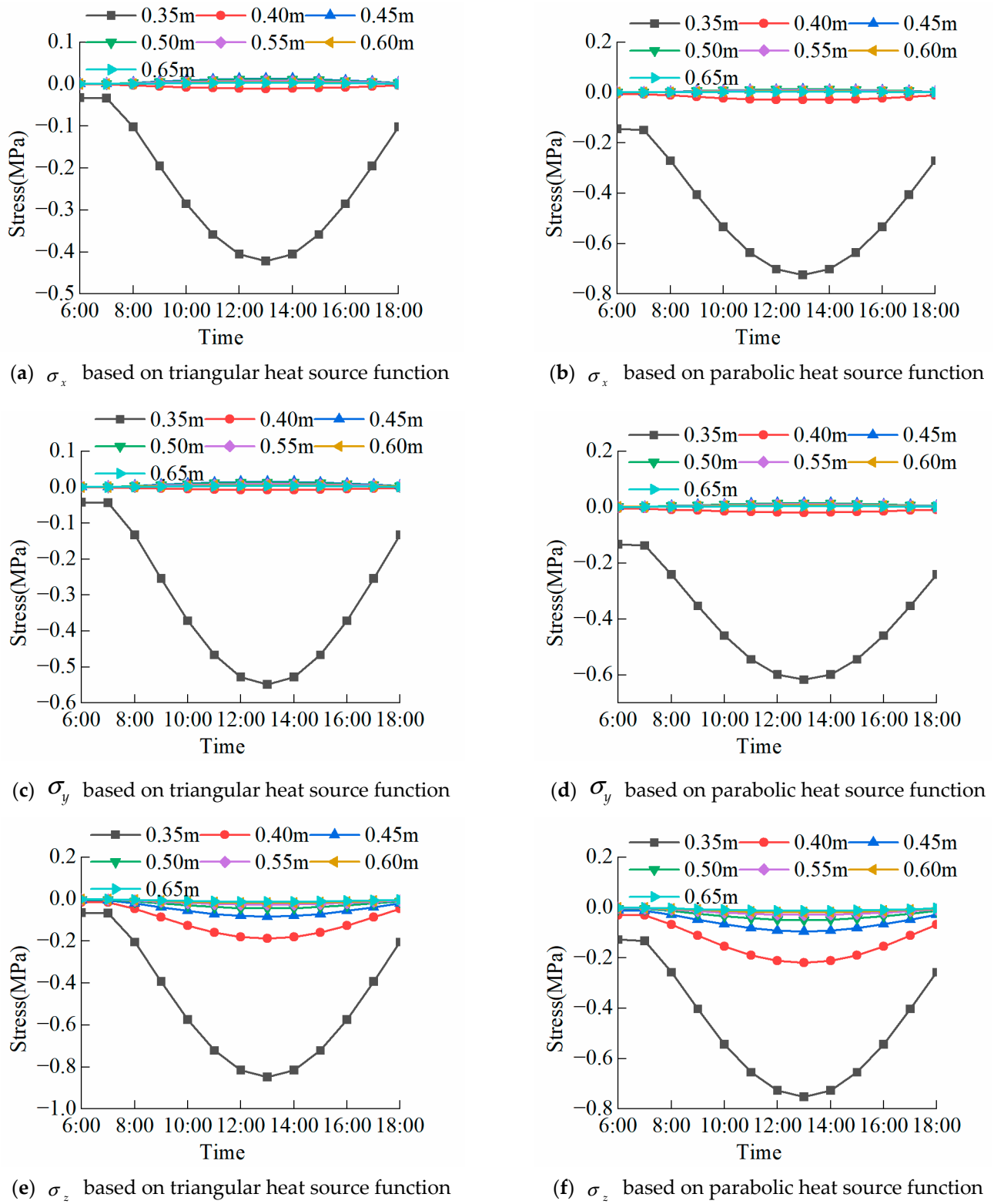
Table 1. Granite properties.

Density ($kg \cdot m^{-3}$)	Heat Capacity ($J \cdot kg^{-1} \cdot K^{-1}$)	Thermal Conductivity ($W \cdot m^{-1} \cdot K^{-1}$)	Elastic Modulus (MPa)	Poisson's Ratio	Thermal Expansion Coefficient (K^{-1})
2.6×10^3	1.1×10^3	2.8	4×10^4	0.3	8×10^{-6}

3.1. Thermal Stress Field of Rocks Based on Parabolic and Triangular Heat Source Functions

The thermal stress of fractured rocks under solar radiation is calculated based on parabolic and triangular heat source functions (Figure 5). The fracture length is 0.35 m, and the fracture opening length is 0.14 m. The daily variations in thermal stress based on both functions exhibit trends consistent with that of solar radiation intensity. From 6:00 to 8:00, the solar radiation is weak, and the thermal stress remains nearly constant. From 9:00 to 13:00, the solar radiation gradually increases, and the thermal stress increases sharply initially and then stabilizes, reaching its maximum value at 13:00. From 14:00 to 18:00, the solar radiation gradually decreases, and the thermal stress decreases accordingly.

At the depths ranging from 0.35 m to 0.65 m below the fracture tip along the z direction of the original coordinate, the maximum daily value of the horizontal stress parallel to the fracture σ_x decreases from 0.42 MPa to approximately 0 MPa, the maximum daily value of the horizontal stress perpendicular to the fracture σ_y decreases from 0.55 MPa to 0 MPa, and the maximum daily value of the vertical stress σ_z decreases from 0.85 MPa to 0.01 MPa based on the triangular heat source function. Correspondingly, the maximum daily value of σ_x decreases from 0.72 MPa to 0 MPa, σ_y decreases from 0.62 MPa to 0 MPa, and σ_z decreases from 0.75 MPa to 0.01 MPa based on the parabolic heat source function. In exposed rock under solar radiation, a fracture acts as a line heat source to the rock, altering the internal heat conduction law and redistributing the thermal stress field of the rock. Compared with a triangular heat source function, the values of σ_x and σ_y are larger and the value of σ_z is smaller at the fracture tip based on a parabolic heat source function. As the depth increases, the thermal stress values based on both functions approach each other, decreasing sharply and eventually tending to 0. The triangular fracture heat source assumes a uniform energy density along its two sides, while the parabolic fracture heat source assumes concentrated energy density at the tip. Therefore, the values of the thermal stress are larger at a fracture tip based on a parabolic heat source function. When analyzing the thermal stability of fractured rocks under solar radiation, the parabolic heat source function provides a more conservative estimate of thermal stress.



(**a**) σ_x based on triangular heat source function

(**b**) σ_x based on parabolic heat source function

(**c**) σ_y based on triangular heat source function

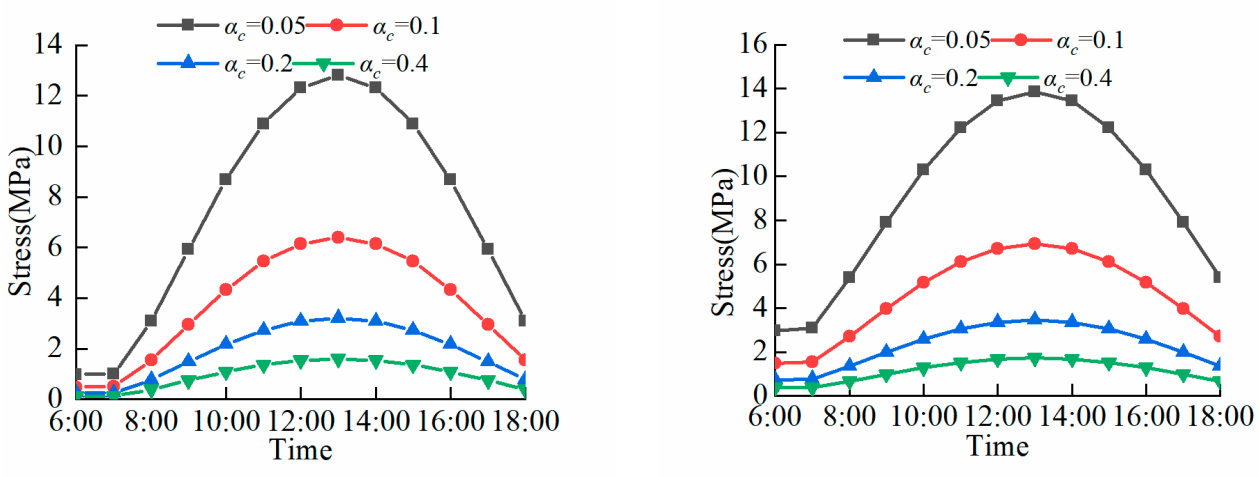
(**d**) σ_y based on parabolic heat source function

(**e**) σ_z based on triangular heat source function

(**f**) σ_z based on parabolic heat source function

Figure 5. Thermal stress–time curve of fractured rock.

Figure 6 shows the maximum circumferential tensile stress $\sigma_{\theta\max}$ near a fracture tip based on the triangular and parabolic heat source functions. The $\sigma_{\theta\max}$ near a fracture tip is analyzed using relative critical size $\alpha_c = \sqrt{2r_c/L}$ when the value of r_c is considered, and the results are equivalent when α_c approaches 0.



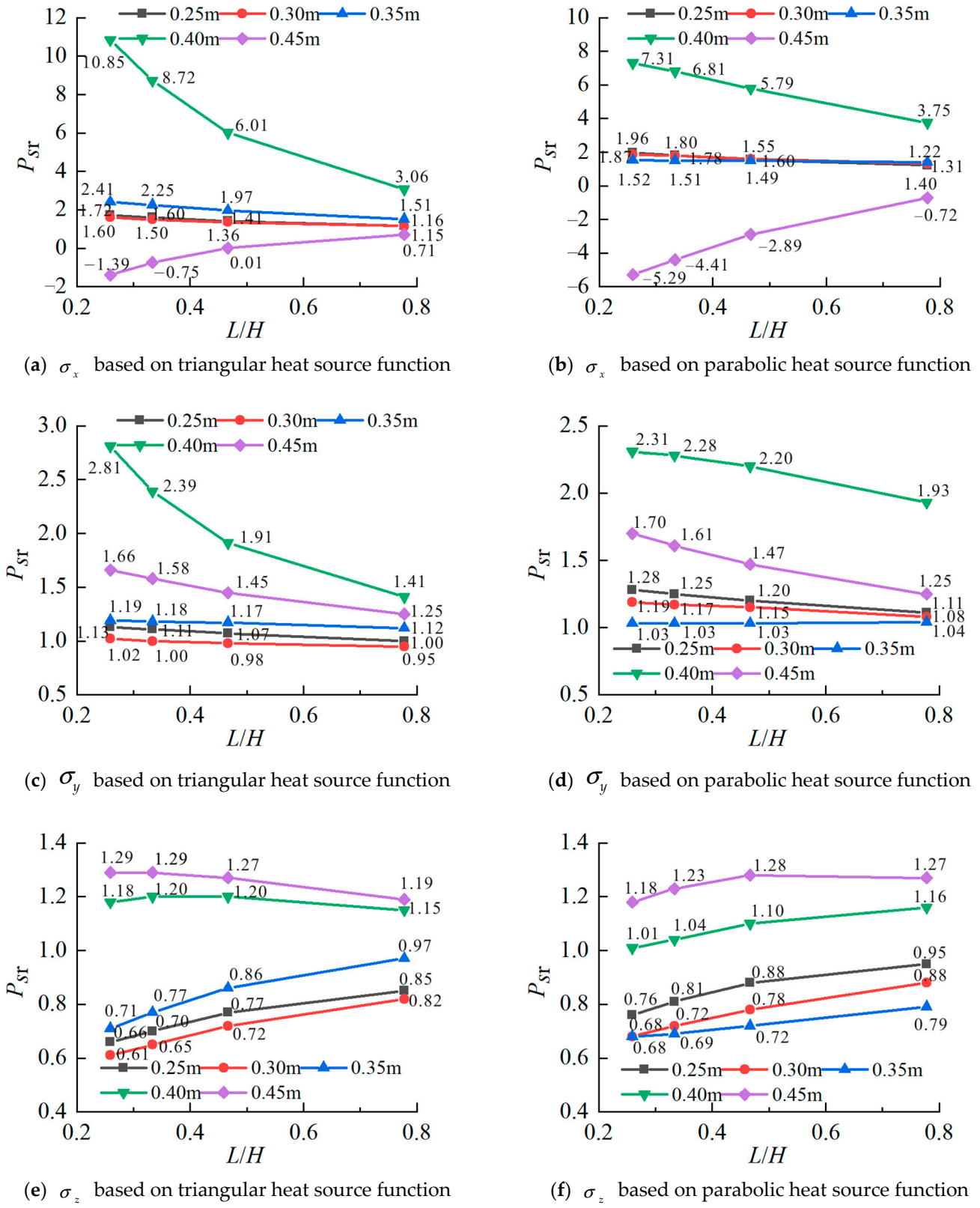
(**a**) Triangular heat source function (**b**) Parabolic heat source function

Figure 6. $\sigma_{\theta max}$ of fractured rock.

During the solar radiation period, the value of $\sigma_{\theta max}$ near a fracture tip based on both functions increases first and then decreases, reaching the maximum value at 13:00. Smaller values of the relative critical size α_c correspond to higher $\sigma_{\theta max}$ values, indicating greater variation rates and daily amplitudes of $\sigma_{\theta max}$ in close proximity to the fracture tip. Compared with a triangular heat source function, the $\sigma_{\theta max}$ when based on a parabolic heat source function is larger, and, as the relative critical size α_c increases, the values of $\sigma_{\theta max}$ for both functions approach each other.

3.2. Influence of Geometric Parameters of Fracture Shape on Thermal Stress

To analyze the influence of the geometric parameters of the fracture shape on the values of the thermal stress based on typical fracture heat source functions, the thermal stress of fractured rocks with different fracture opening lengths (H = 0.15, 0.45, 0.75, 1.05, 1.35 m) and a constant fracture length L of 0.35 m (L/H = 2.33, 0.78, 0.47, 0.33, 0.26) is calculated based on the triangular heat source function and the parabolic heat source function. The stress ratio P_{sr} is the ratio of thermal stress at the fracture tip with different fracture opening lengths H to that of H = 0.15 m. Since the thermal stress is the maximum at 13:00 during the solar radiation period, the variation in thermal stress along a depth from 0.25 m to 0.45 m below the fracture tip in the z direction of the original coordinate at this time is analyzed, as shown in Figures 7 and 8. For both heat source functions, the horizontal stress parallel to the fracture σ_x and the horizontal stress perpendicular to the fracture σ_y increase as the ratio of fracture length to fracture opening length (L/H) decreases. The vertical stress σ_z near the fracture tip decreases as L/H decreases and with increasing depth; σ_z first increases and then decreases as L/H decreases. The variation in thermal stress decreases with L/H as the depth increases. The maximum circumferential tensile stress $\sigma_{\theta max}$ near a fracture tip increases as L/H decreases, and the variation in $\sigma_{\theta max}$ decreases with L/H as the relative critical size α_c increases. The influence of L/H on thermal stress is most significant at the fracture tip. Compared with the parabolic heat source function, the thermal stress values based on triangular heat source function change greatly with the increase in L/H, indicating that the variation in fracture shape geometric parameter L/H has a more significant influence on thermal stress values based on triangular heat source function.



(**a**) σ_x based on triangular heat source function

(**b**) σ_x based on parabolic heat source function

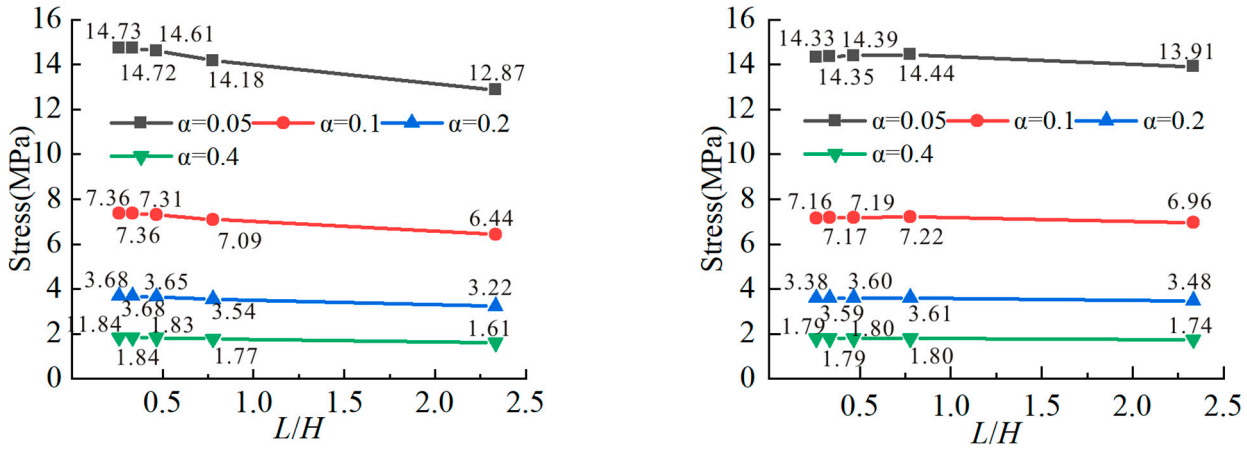
(**c**) σ_y based on triangular heat source function

(**d**) σ_y based on parabolic heat source function

(**e**) σ_z based on triangular heat source function

(**f**) σ_z based on parabolic heat source function

Figure 7. Influence of geometric parameters of fracture shape on thermal stress of rock at 13:00.

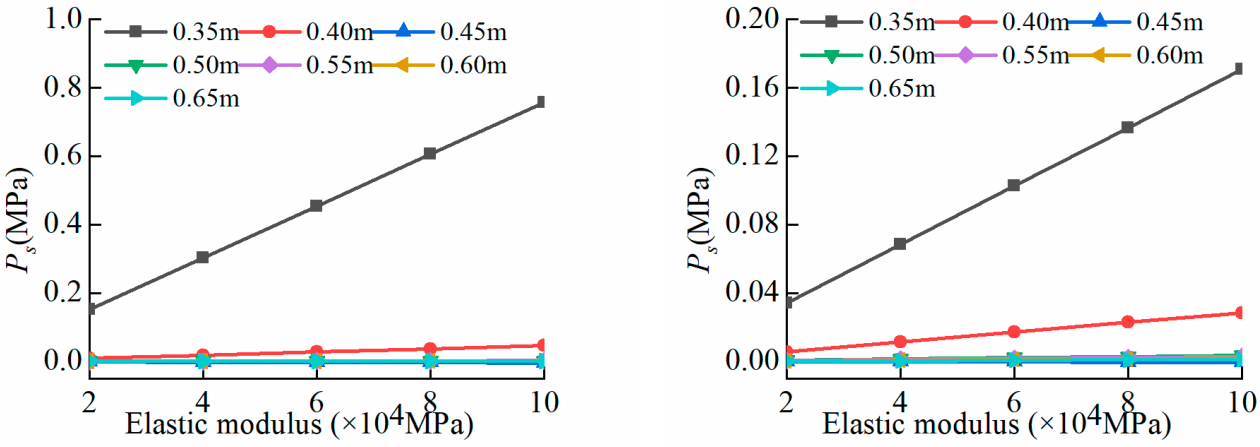


(**a**) Triangular heat source function (**b**) Parabolic heat source function

Figure 8. Influence of geometric parameters of fracture shape on $\sigma_{\theta\max}$ at 13:00.

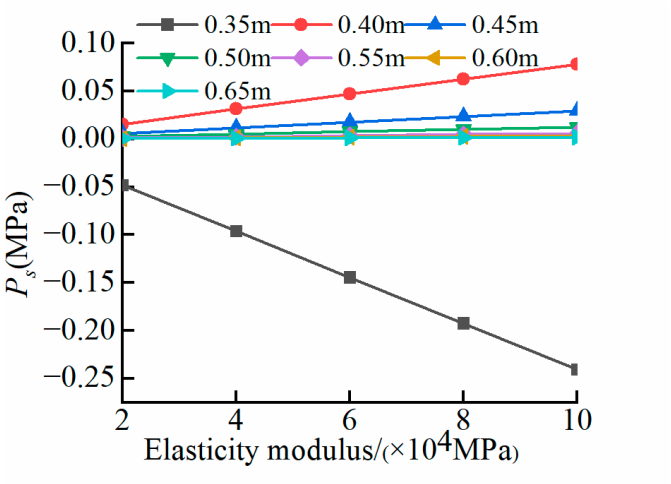
3.3. Applicability Analysis of Fracture Heat Source Functions

Although natural fracture shapes are usually irregular, the resulting thermal stress fields exhibit regular shapes during heat transfer in exposed fractured rocks in tunnel engineering. Thus, triangular and parabolic fracture heat source functions serve as simplified yet effective models for the analytical calculation of thermal stress fields of fractured rocks under solar radiation. The thermodynamic parameters of rocks have a significant impact on thermal stress. To evaluate the applicability of fracture heat source functions for analyzing the thermal stress field of rocks with different thermodynamic properties, the thermal stress of fractured rocks with different elastic moduli, Poisson's ratios, thermal expansion coefficients, thermal conductivities, densities, and heat capacities at 13:00 is calculated based on the triangular and parabolic fracture heat source functions. The stress difference P_s is defined as the difference in thermal stress at the same depth based on the parabolic and triangular heat source functions, and the stress difference P_{sm} is defined as the difference in the maximum circumferential tensile stress $\sigma_{\theta\max}$ at the same relative critical size α_c based on the parabolic and triangular heat source functions, as shown in Figures 9–14.

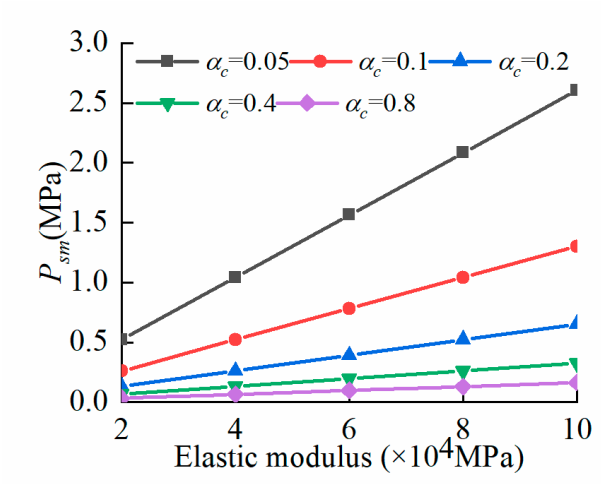


(**a**) Stress difference P_s of σ_x (**b**) Stress difference P_s of σ_y

Figure 9. *Cont.*

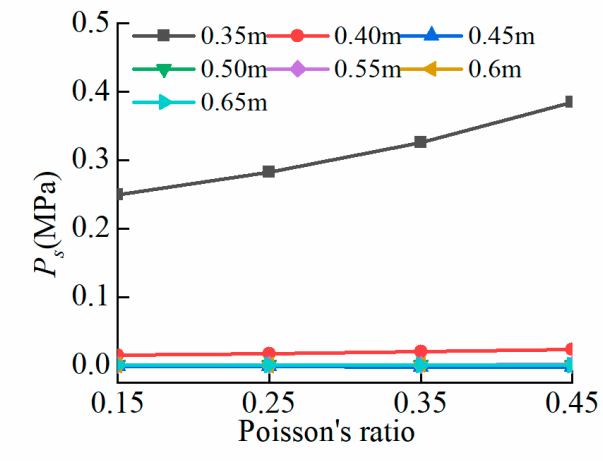


(**c**) Stress difference P_s of σ_z

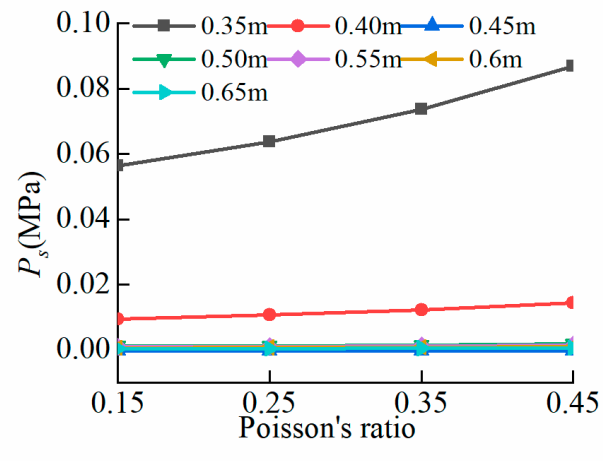


(**d**) Stress difference P_{sm} of $\sigma_{\theta max}$

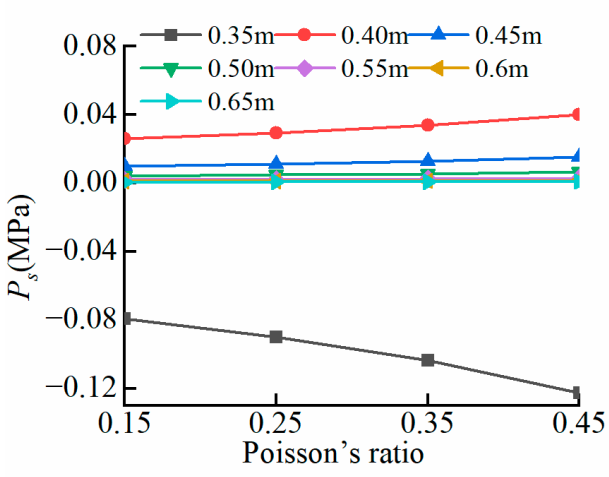
Figure 9. Influence of elastic modulus on thermal stress of rock.



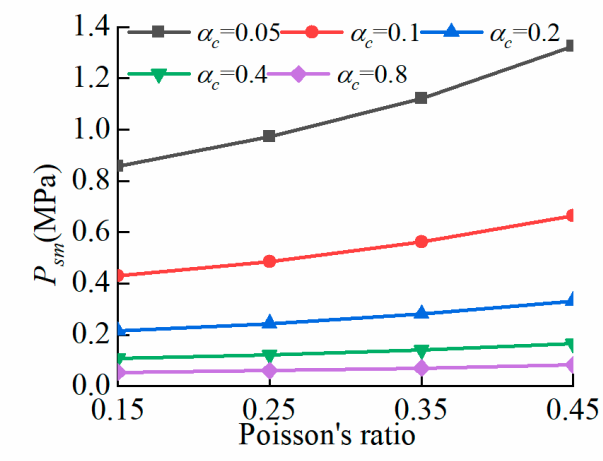
(**a**) Stress difference P_s of σ_x



(**b**) Stress difference P_s of σ_y

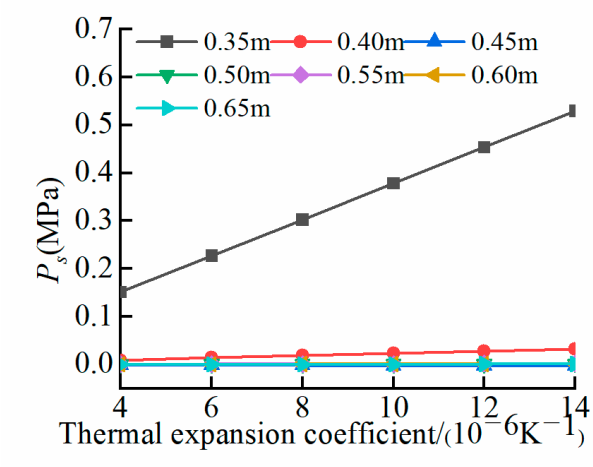


(**c**) Stress difference P_s of σ_z

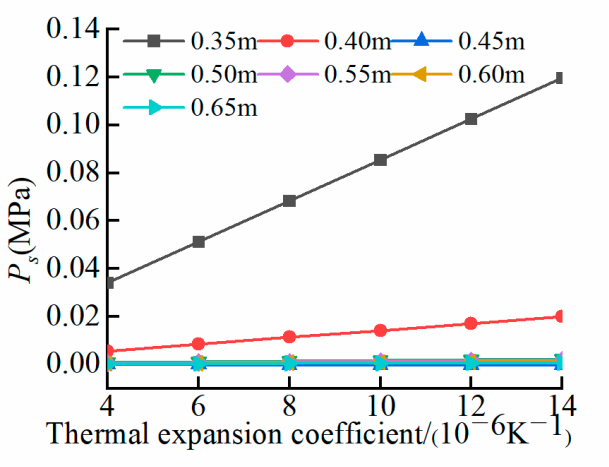


(**d**) Stress difference P_{sm} of $\sigma_{\theta max}$

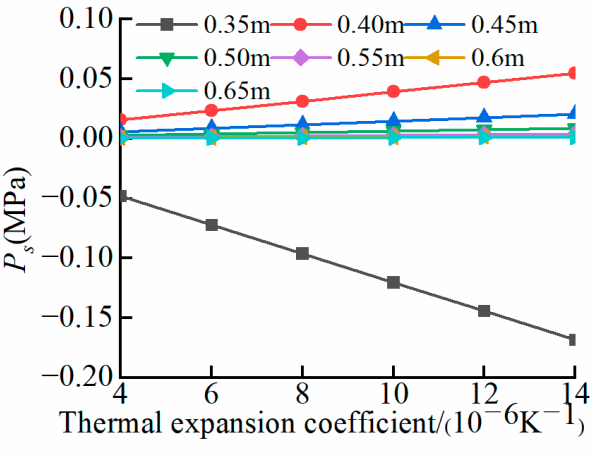
Figure 10. Influence of Poisson's ratio on thermal stress of rock.



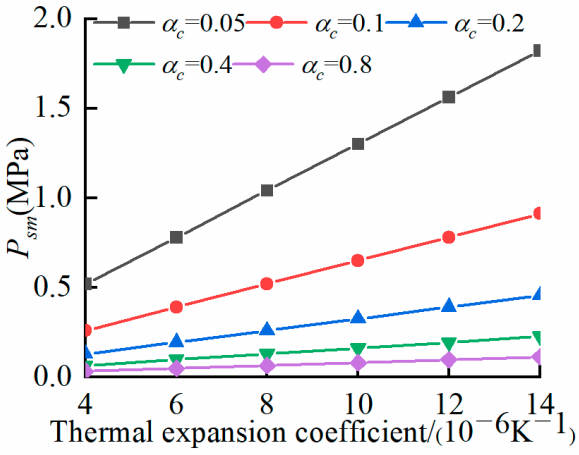
(**a**) Stress difference P_s of σ_x



(**b**) Stress difference P_s of σ_y

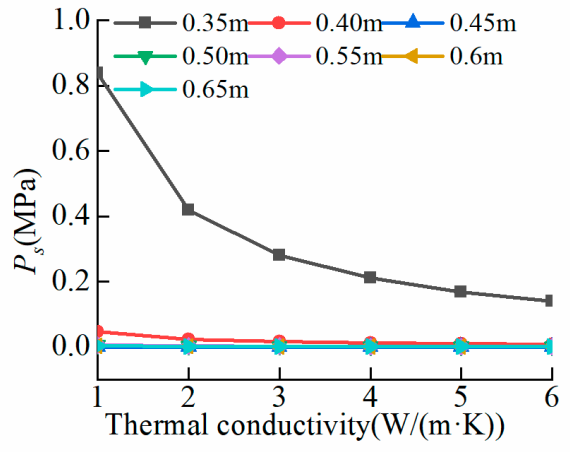


(**c**) Stress difference P_s of σ_z

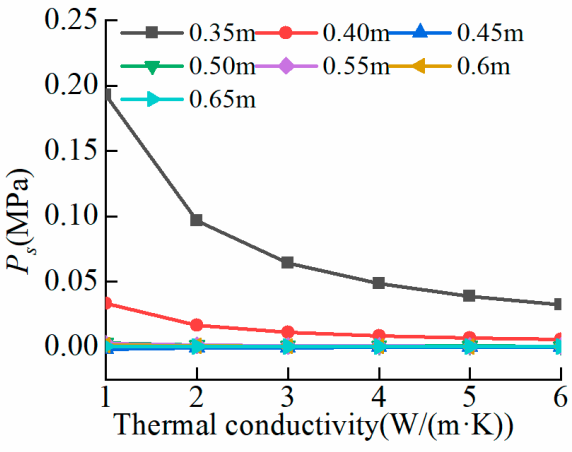


(**d**) Stress difference P_{sm} of $\sigma_{\theta max}$

Figure 11. Influence of thermal expansion coefficient on thermal stress of rock.

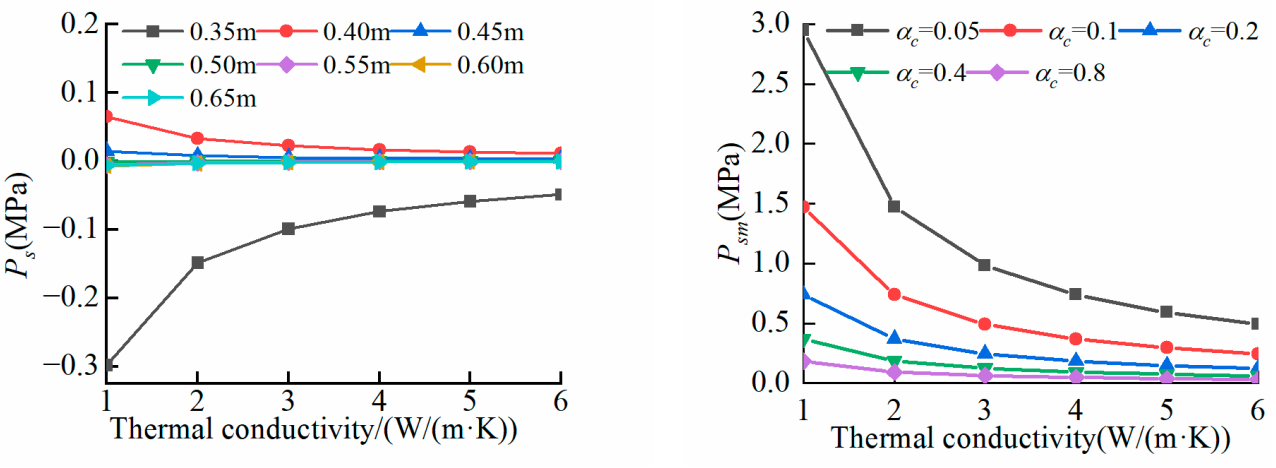


(**a**) Stress difference P_s of σ_x



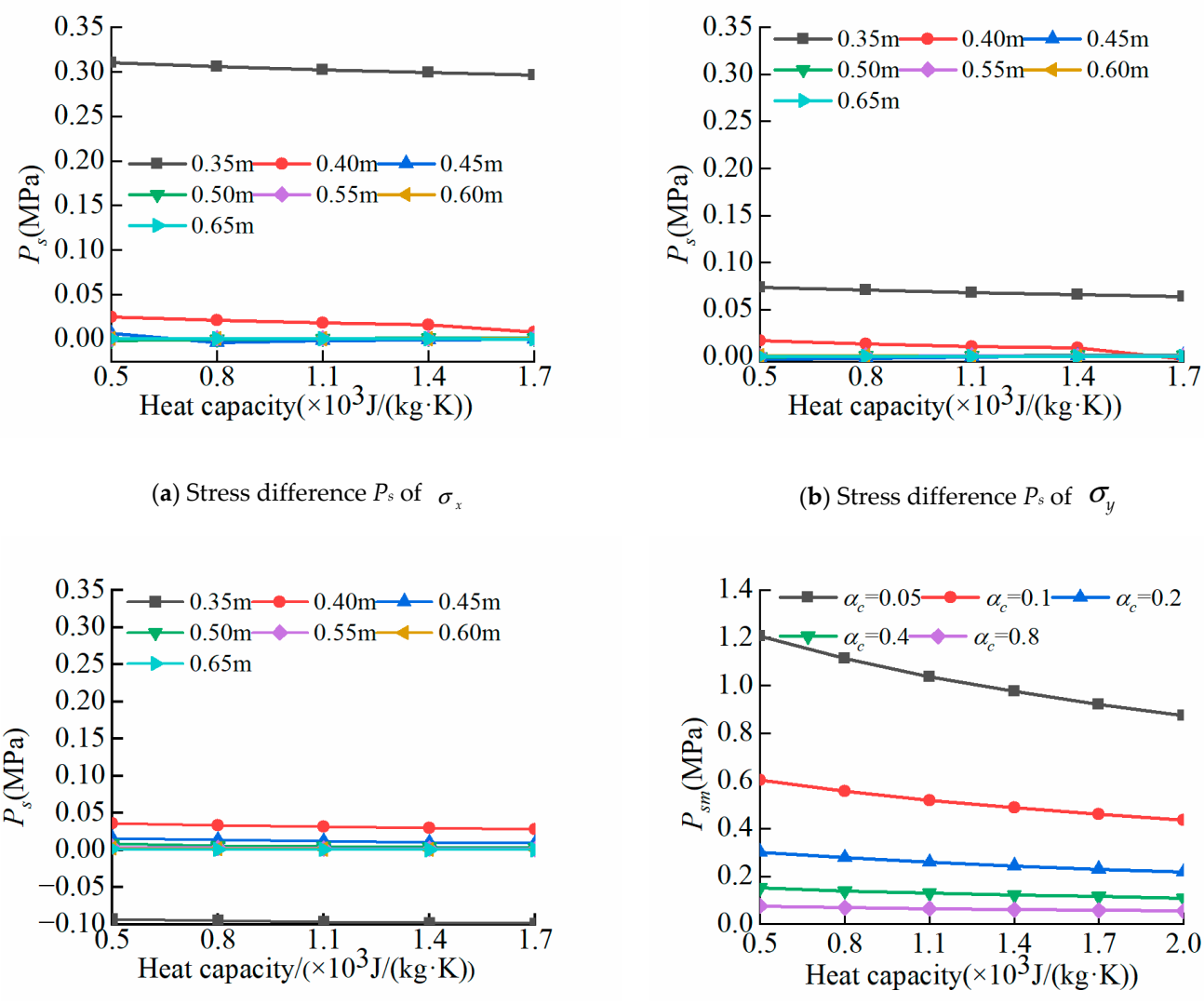
(**b**) Stress difference P_s of σ_y

Figure 12. *Cont.*



(**c**) Stress difference P_s of σ_z (**d**) Stress difference P_{sm} of $\sigma_{\theta max}$

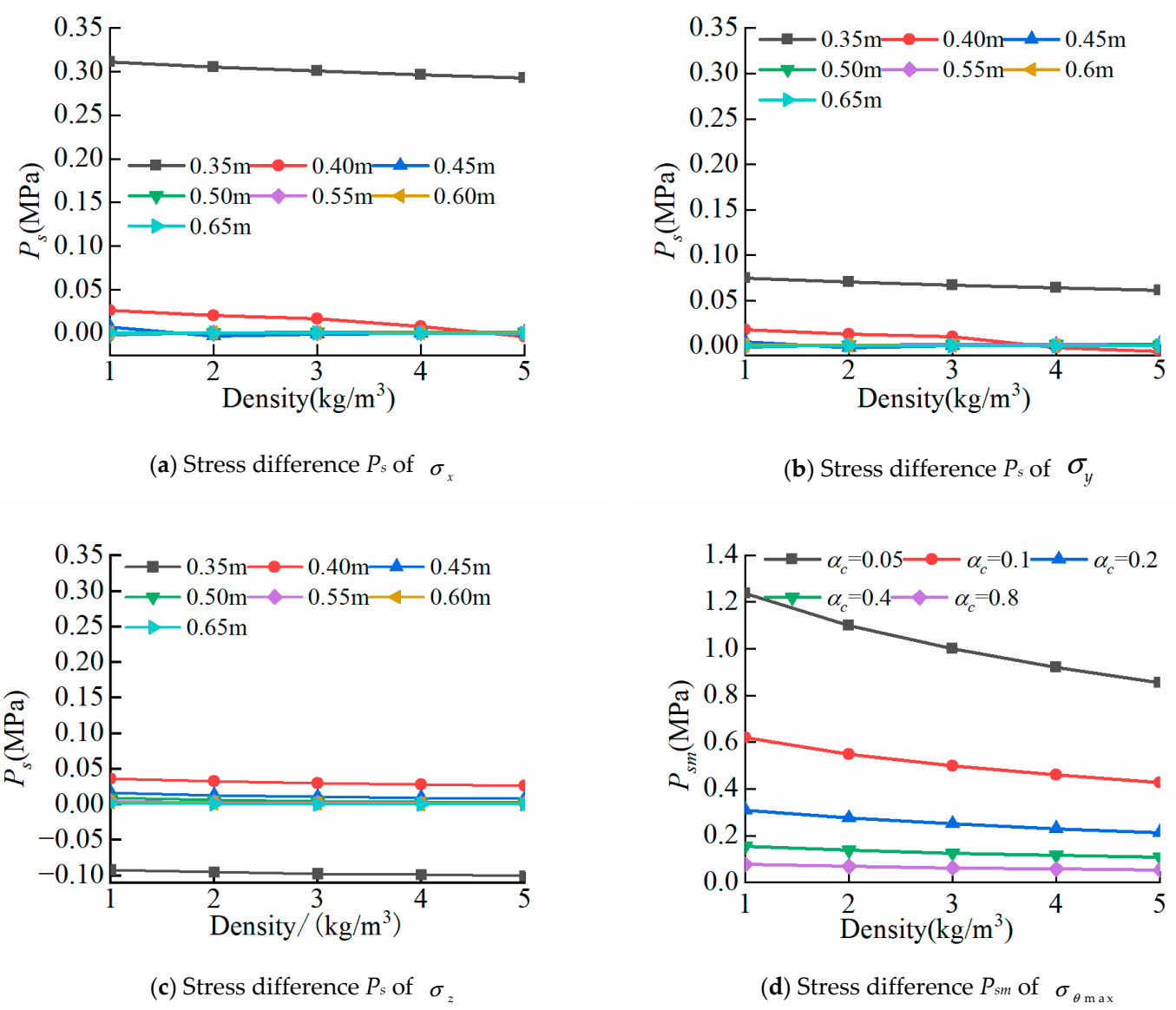
Figure 12. Influence of thermal conductivity on thermal stress of rock.



(**a**) Stress difference P_s of σ_x (**b**) Stress difference P_s of σ_y

(**c**) Stress difference P_s of σ_z (**d**) Stress difference P_{sm} of $\sigma_{\theta max}$

Figure 13. Influence of heat capacity on thermal stress of rock.



(**a**) Stress difference P_s of σ_x

(**b**) Stress difference P_s of σ_y

(**c**) Stress difference P_s of σ_z

(**d**) Stress difference P_{sm} of $\sigma_{\theta max}$

Figure 14. Influence of density on thermal stress of rock.

The elastic modulus of rock varies from 1×10^4 MPa to 1×10^5 MPa. In the parameter analysis, the elastic modulus is set as E = (1×10^4, 2×10^4, 3×10^4, 4×10^4, 5×10^4, 6×10^4, 7×10^4, 8×10^4, 9×10^4, 1×10^5) MPa, and the variations in stress differences P_s and P_{sm} with the elastic modulus are shown in Figure 9. It is shown that P_s and P_{sm} increase with the elastic modulus, reaching their maximum values at the fracture tip and decreasing gradually to 0 as the distance from the fracture tip increases. Hard rocks, characterized by high elastic moduli, typically exhibit brittle fracture behavior, resulting in nearly ideal sharp fractures. Therefore, the triangular heat source function is more appropriate for hard rocks. In contrast, soft rocks possess lower mechanical strengths and elastic moduli. During fracturing, plastic deformation leads to blunting of plastic deformation, resulting in a certain radius of curvature. Therefore, the parabolic heat source function is more suitable for soft rocks.

The thermal expansion coefficient of rock varies from 4×10^{-6} K^{-1} to 14×10^{-6} K^{-1}. In the parameter analysis, the thermal expansion coefficient is set as α = (4×10^{-6}, 6×10^{-6}, 8×10^{-6}, 10×10^{-6}, 12×10^{-6}, 14×10^{-6}) K^{-1}. The thermal conductivity affects the rock's temperature field and indirectly affects the rock's thermal stress field. The thermal conductivity is set as λ = (1, 2, 3, 4, 5, 6) W/(m·K). The influences of the thermal

expansion coefficient and thermal conductivity on stress differences P_s and P_{sm} are shown in Figures 11 and 12. It is shown that P_s and P_{sm} decrease with the increase in thermal conductivity and increase with the increase in thermal expansion coefficient. Variations in mineral composition and structure among different rock types lead to significant differences in their thermodynamic properties. For rocks with low thermal conductivity and high thermal deformability, the thermal stresses computed using the triangular and parabolic heat source functions differ significantly. As a result, it is reasonable to choose heat source function based on the mechanical properties of the rock and the actual fracture shape. For rocks with good thermal conductivity and small thermal deformation, the values of thermal stress based on the parabolic heat source function are more conservative.

The influences of Poisson's ratio, heat capacity, and density on stress differences P_s and P_{sm} are shown in Figures 10, 13 and 14. It is shown that variations in Poisson's ratio, heat capacity, and density have little impact on P_s and P_{sm}, and the thermal stress at the fracture tip based on triangular and parabolic heat source functions differs little.

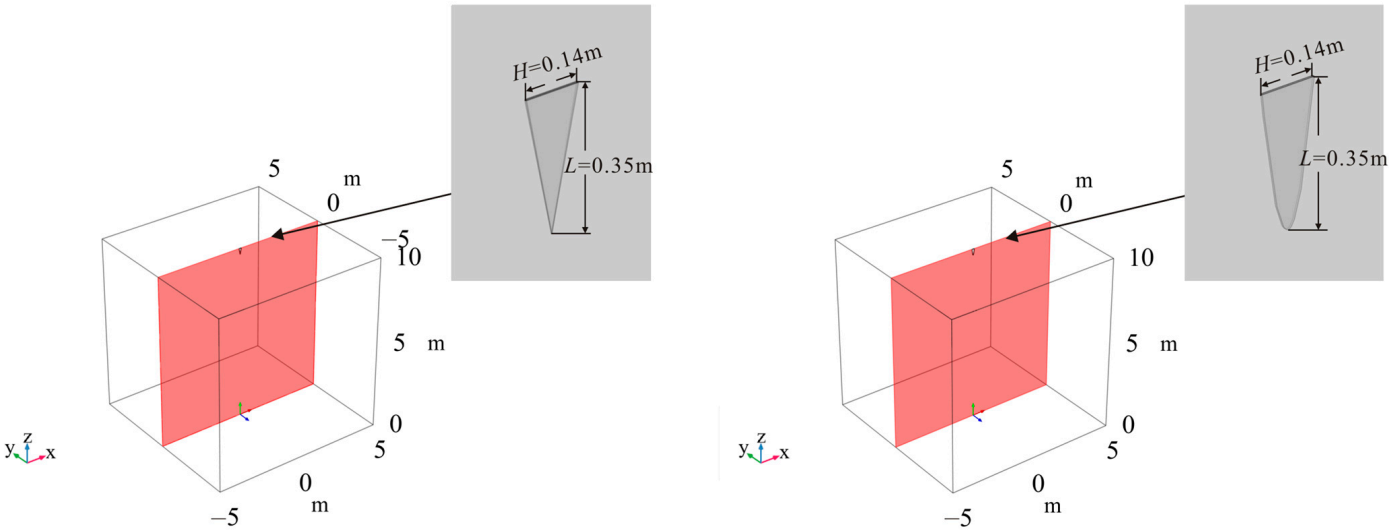
The parabolic fracture heat source function provides a valuable tool for assessing the thermal stress field of rocks with different thermodynamic properties. Therefore, it is a typical function for analyzing thermal effects of fractured rocks under solar radiation.

4. Finite Element Analysis of Thermal Stress Field of Rocks with Typical Fracture Heat Sources

Using finite element method and COMSOL-MULTIPHYSICS 5.5 software, a model is established to analyze the thermal stress field of rocks with different fracture heat sources under solar radiation.

4.1. Parameters of Finite Element Analysis

A finite element model with dimensions of 10 m × 10 m × 10 m is established to represent fractured rock under solar radiation. There is a triangular and parabolic fracture heat source along the z direction at the upper boundary, with L = 0.35 m and H = 0.14 m, as shown in Figure 15. The model dimensions are significantly larger than those of the heat source, thus approximating a semi-infinite rock with a fracture heat source. The environmental parameters and granite parameters are shown in Figure 4 and Table 1. The initial and boundary conditions applied in the finite element analysis are consistent with those used in the theoretical analytical model. The initial condition is the initial temperature of the rock (original rock temperature). The boundary condition is the heat exchange between the upper surface of the model and the external environment. The remaining external surfaces are treated as adiabatic boundaries. The fracture heat source boundary is the radiation energy absorbed by the fracture. The bottom boundary is assigned a fixed constraint, while the remaining boundaries are free to displace under thermal expansion and contraction [29]. The governing equations for heat transfer and thermal stress are based on Fourier's law of heat conduction and the equilibrium differential equations, respectively. The solid heat transfer module, surface-to-surface radiation module, and solid mechanics module are used to analyze the evolution of the thermal stress field.

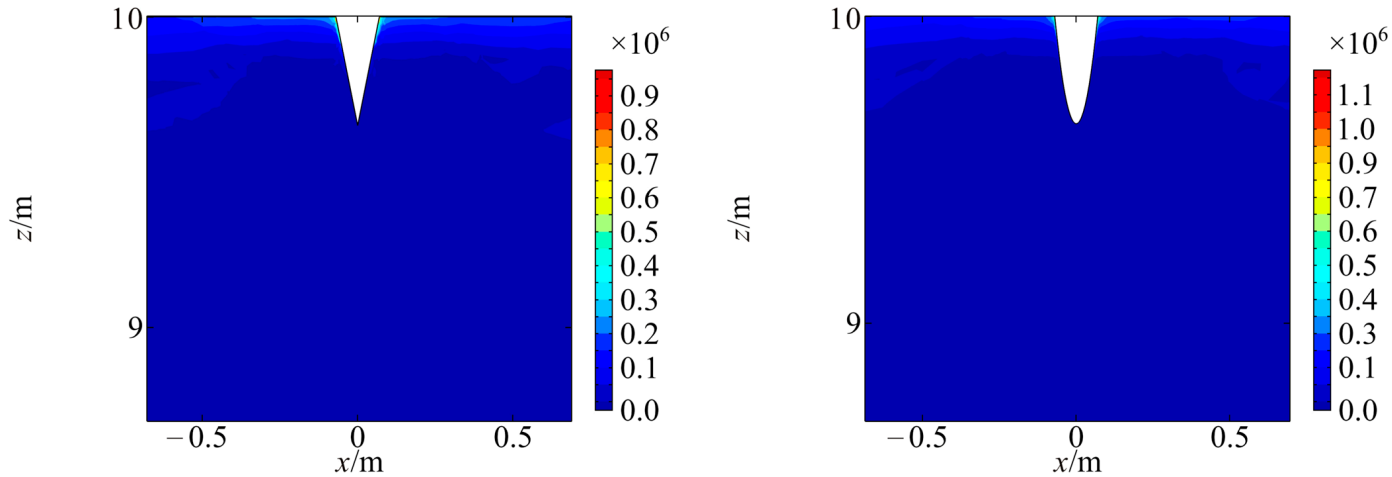


(**a**) Triangular heat source function (**b**) Parabolic heat source function

Figure 15. Model of finite element analysis.

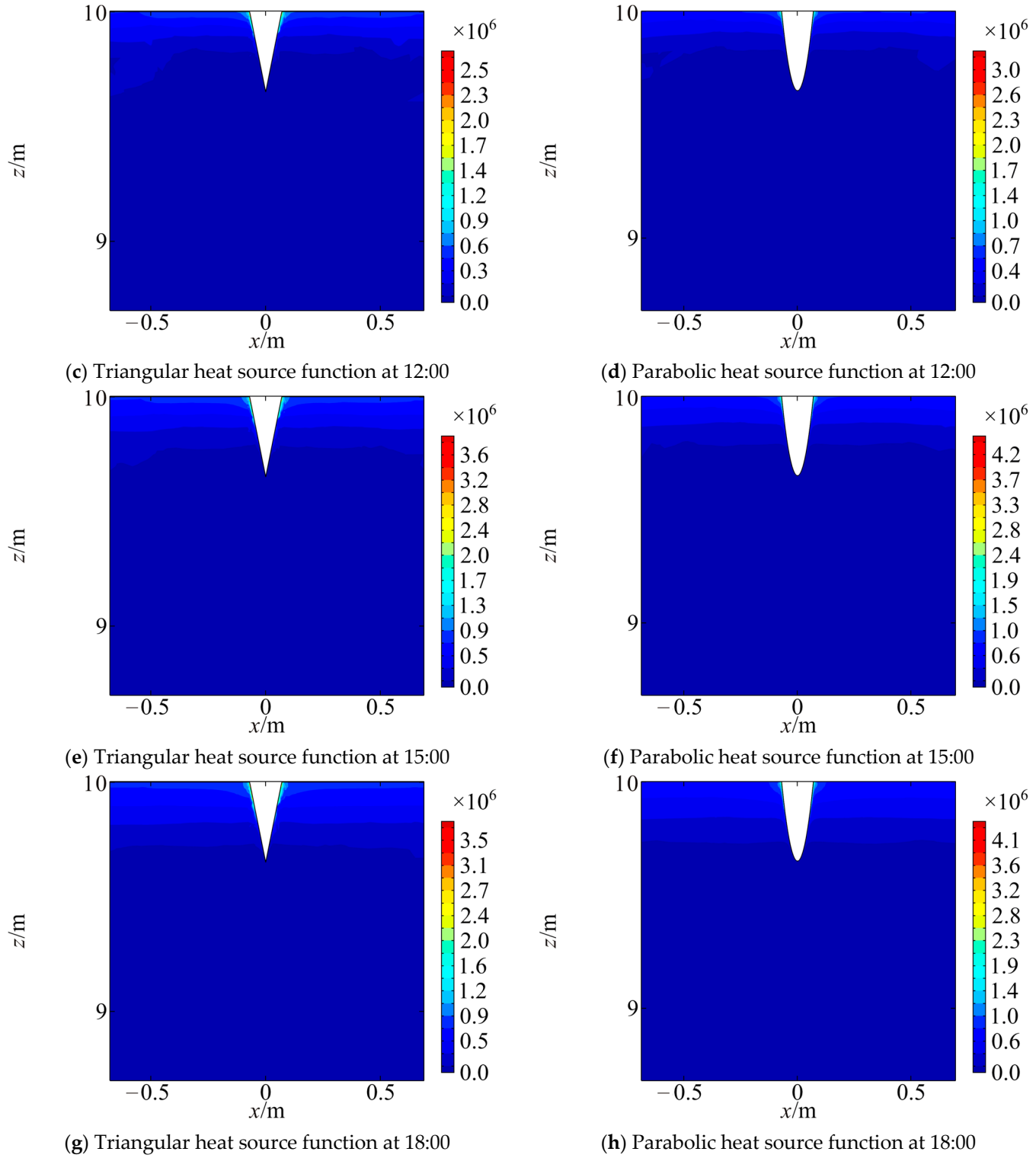
4.2. Thermal Stress Field of Fractured Rocks

The thermal stress fields of rocks with triangular and parabolic fracture heat sources under solar radiation are shown in Figure 16. Analysis of the fracture section indicates an increase in thermal stress around the fracture. The parabolic heat source model yields higher thermal stresses at the fracture tips compared to the triangular model. As the depth increases, the thermal stress values based on both functions approach each other. The numerical simulation results are consistent with the theoretical analysis, verifying the accuracy of the model. However, due to the use of a finite rock to simulate an infinite rock in the numerical model, there is stress concentration at the boundaries, which leads to differences between the numerical model and the theoretical analysis.



(**a**) Triangular heat source function at 9:00 (**b**) Parabolic heat source function at 9:00

Figure 16. *Cont.*



(**c**) Triangular heat source function at 12:00

(**d**) Parabolic heat source function at 12:00

(**e**) Triangular heat source function at 15:00

(**f**) Parabolic heat source function at 15:00

(**g**) Triangular heat source function at 18:00

(**h**) Parabolic heat source function at 18:00

Figure 16. Thermal stress field of fractured rock (unit: Pa).

5. Discussion

This study focused on granite and established a parabolic shape function method for the thermal stress field near the fracture tip under solar radiation. The advantages and applicable conditions of this parabolic function, in comparison to the triangular function, were elucidated. Although the parameter analysis focused on granite, the relationship between rock's thermal properties (e.g., elastic modulus, thermal conductivity, and thermal expansion coefficient) and the applicability of the heat source shape function, along with

the underlying physical mechanism, exhibit universality. The findings provide a theoretical basis for extending this method to other rock types, including sandstone with high porosity and significant thermal expansion, limestone with well-developed bedding and low thermal conductivity, basalt with columnar joints, and low-strength and easily deforming shale. Although variations in mineral composition, structure, porosity, and thermal–physical–mechanical properties among rock types (e.g., the possible lower thermal conductivity of sandstone and the significant influence of quartz content on the thermal expansion coefficient; the small elastic modulus and poor thermal conductivity of shale) influence the distribution of thermal stress and the selection of the optimal function, the proposed analytical framework and core of the methodology remain applicable. Consequently, the results of this study not only provide a basis for the prevention of thermal damage at tunnel entrances but also hold potential for broader applications: (1) Rock slope stability assessment: the expansion of fractures, block loosening, and the risk of surface spalling in shallow rock layer induced by thermal stress cycles in strong sunlight areas (such as in southern China) can be predicted. (2) Stone heritage conservation: thermal stresses can be accurately assessed at the surface and fracture tips in stone caves, cliff carvings, and stone tablets exposed to solar radiation, thereby elucidating mechanisms of thermal weathering and exfoliation to guide protective strategies. (3) The proposed method can be applied in engineering fields involving thermal coupling of high-temperature rocks (e.g., geothermal energy, nuclear waste disposal).

Future work should include parameter validation for diverse rock types, refinement of function selection criteria, and investigation of the influence of additional factors such as moisture, dynamic solar loading, and 3D fracture network.

6. Conclusions

In this study, a parabolic shape function for the heat source and thermal stress at the fracture tip of rocks is proposed, and the thermal stress field of fractured rocks under solar radiation is calculated based on typical fracture heat source functions. The applicability of different heat source functions for analyzing the effects of heat on rocks with different thermodynamic properties is discussed. The main conclusions are as follows:

(1) The daily variation trends in thermal stress based on triangular and parabolic heat source functions are consistent. Compared with the triangular heat source function, the values of thermal stress at fracture tip are larger, and the daily maximum $\sigma_{\theta\max}$ increases by 8.14% when $\alpha_c = 0.05$ based on the parabolic heat source function. When analyzing thermal stability of fractured rocks under solar radiation, parabolic heat source function provides more conservative estimations of thermal stress.

(2) Based on both heat source functions, the horizontal stresses σ_x and σ_y increase as the ratio of fracture length to fracture opening length (L/H) decreases, while the vertical stress σ_z decreases as L/H decreases, and the maximum circumferential tensile stress $\sigma_{\theta\max}$ at fracture tip increases as L/H increases. Compared with parabolic heat source function, the thermal stress values based on triangular heat source function change larger as L/H increases, indicating that the variation in fracture shape geometric parameter L/H has a more significant effect on the thermal stress values based on the triangular heat source function.

(3) The applicability of fracture heat source functions is analyzed. For soft rocks and those with good thermal conductivity and small thermal deformation, the parabolic heat source function is more reasonable. For hard rocks, the triangular heat source function is more appropriate. The parabolic fracture heat source function provides a valuable framework for analyzing the thermal stress field of rocks with diverse thermodynamic

properties, which is a typical method for analyzing the thermal effects of fractured rocks under solar radiation.

(4) Thermal stress fields of rocks with triangular and parabolic fracture heat sources under solar radiation are analyzed by numerical simulation. Results indicate an increase in thermal stress around the fracture. Compared with triangular heat source, the thermal stress at fracture tip is larger with parabolic heat source. As the depth increases, the thermal stress values of both functions approach each other.

Author Contributions: W.C. conceived this research project. Y.W. and W.C. designed a detailed research plan for the present study. Y.W. and W.C. conducted the data analysis. Y.W. wrote this manuscript. Both authors reviewed the manuscript. All authors have read and agreed to the published version of the manuscript.

Funding: This research was funded by the "Special Funds for Basic Research of Central Public Welfare Research Institutes" of the China Academy of Cultural Heritage (2024-JBKY-14), the Open Fund of Technology Innovation Center for Risk Prevention and Control of Major Project Geosafety, Ministry of Natural Resources (TICRPC-2024-03) and the National Natural Science Foundation of China (NSFC; 51978039).

Data Availability Statement: The original contributions presented in this study are included in the article. Further inquiries can be directed to the corresponding author.

Conflicts of Interest: The authors declare no conflicts of interest.

References

1. Guerin, A.; Jaboyedoff, M.; Collins, B.D.; Stock, G.M.; Derron, M.; Abellán, A.; Matasci, B. Remote thermal detection of exfoliation sheet deformation. *Landslides* **2020**, *18*, 865–879. [CrossRef]
2. Loope, D.B.; Loope, G.R.; Burberry, C.M.; Rowe, C.M.; Bryant, G.C. Surficial fractures in the Navajo Sandstone, Southwestern USA: The roles of thermal cycles, rainstorms, granular disintegration, and iterative cracking. *Earth Surf. Process. Landf.* **2020**, *45*, 2063–2077. [CrossRef]
3. Karoline, M.; Heather, V.; Jan-christoph, O.; Andreas, E.; Richard, D. Linking rock weathering, rockwall instability and rockfall supply on talus slopes in glaciated hanging valleys (Swiss Alps). *Permafr. Periglac. Process.* **2018**, *29*, 135–151. [CrossRef]
4. Gunzburger, Y.; Merrirn-Soukatchoff, V. Near-surface temperatures and heat balance of bare outcrops exposed to solar radiation. *Earth Surf. Process. Landf.* **2011**, *36*, 1577–1589. [CrossRef]
5. Smith, B.J.; Srinivasan, S.; Gomez-Heras, M.; Basheer, P.A.M.; Viles, H.A. Near-surface temperature cycling of stone and its implications for scales of surface deterioration. *Geomorphology* **2011**, *130*, 76–82. [CrossRef]
6. Meier, J.; Bock, H. Stability of a block resting on an inclined plane—A classical problem revisited. *Int. J. Rock Mech. Min. Sci.* **2014**, *70*, 407–417. [CrossRef]
7. Zhang, Z.; Wu, Q.; Xun, X. Radiation and energy balance characteristics of asphalt pavement in permafrost regions. *Environ. Earth Sci.* **2016**, *75*, 221. [CrossRef]
8. Aldred, J.; Eppes, M.C.; Aquino, K.; Deal, R.; Garbini, J.; Swami, S.; Tuttle, A.; Xanthos, G. The influence of solar-induced thermal stresses on the mechanical weathering of rocks in humid mid-latitudes. *Earth Surf. Process. Landf.* **2016**, *41*, 603–614. [CrossRef]
9. Ding, W.; Chen, J.; Feng, X.; Zhou, H.; Wang, S. Study on weathering characteristics of surrounding rock in Longmen cavern. *Rock Soil Mech.* **2004**, *25*, 145–148. (In Chinese)
10. Meng, Y.; Yan, Z.; Wang, J.; Ni, P.; Liu, Y. Research on solar radiation characteristics in Vairocana Buddha niche in Longmen Grottoes. *J. Arid Land Resour. Environ.* **2022**, *36*, 129–138. (In Chinese)
11. Wang, Y.; Chen, W. Study on thermal stress field of triangle fracture of granite in high-temperature environment. *Chin. J. Rock Mech. Eng.* **2021**, *40*, 3074–3083. (In Chinese)
12. Xu, D.; Gu, H.; Chen, W.; Liang, X.; Zhang, J.; Wang, Z. Characteristics of thermal stress and vulnerability assessment of Houxu Tablet in Yongyou Temple Mountain Resort. *J. Northwest Univ. Nat. Sci. Ed.* **2021**, *51*, 353–359. (In Chinese)
13. Chen, J.; Wang, J.; Yan, S.; Fang, Y. Analysis on the Cracking Mechanism of the Surface Layer on Huashan Rock Painting in Ningming, Guangxi. *J. Fudan Univ. Nat. Sci.* **2021**, *60*, 157–165. (In Chinese)
14. Collins, B.D.; Stock, G.M. Rockfall triggering by cyclic thermal stressing of exfoliation fractures. *Nat. Geosci.* **2016**, *9*, 395–400. [CrossRef]

15. Wedekind, W.; Gross, C.J.; Hoffmann, A.; Siegesmund, S. Damage phenomenon and petrophysical properties of sandstones at the Phnom Bakheng Temple (Angkor, Cambodia): First investigations and possible conservation measures. *Environ. Geol.* **2018**, *77*, 735.1–735.36. [CrossRef]
16. Amaral Vamaral, E.; Velloso, R.; Chavez, L.; Gusmão, L.; Amaral, C. On the Effect of Thermally Induced Stresses in Failures of Some Rock Slopes in Rio de Janeiro, Brazil. *Rock Mech. Rock Eng.* **2013**, *46*, 123–134. [CrossRef]
17. Wang, Y.; Chen, W. Nonlinear temperature field of granite fracture tip induced by high natural environmental temperature based on fracture shape function. *Rock Soil Mech.* **2022**, *43*, 267–274. (In Chinese)
18. Hu, J.; Li, S.; Li, L.; Shi, S.; Zhou, Z.; Liu, H.; He, P. Field, experimental, and numerical investigation of a rockfall above a tunnel portal in southwestern China. *Bull. Eng. Geol. Environ.* **2018**, *77*, 1365–1382. [CrossRef]
19. Wu, W.; Zhu, H.; Lin, J.S.; Zhang, X.; Ma, G. Tunnel stability assessment by 3D DDA-keyblock analysis. *Tunn. Undergr. Space Technol.* **2018**, *71*, 210–214. [CrossRef]
20. Alam, M.R.; Munaswamy, K.; Swamidas, A.S.J. Experimental and numerical studies on dynamic crack growth in layered slate rock under wedge impact loads: Part II—Non-plane strain problem. *Fatigue Fract. Eng. Mater. Struct.* **2007**, *30*, 915–931. [CrossRef]
21. Ayatollahi, M.R.; Torabi, A.R. Determination of mode II fracture toughness for U-shaped notches using Brazilian disc specimen. *Int. J. Solids Struct.* **2010**, *47*, 454–465. [CrossRef]
22. Ayatollahi, M.R.; Torabi, A.R. Brittle fracture in rounded-tip V-shaped notches. *Mater. Des.* **2010**, *31*, 60–67. [CrossRef]
23. Chen, Y.Z.; Wang, Z.X.; Lin, X.Y. Refinement for stress intensity factor solution for a parabolic-shaped crack from the perturbation method. *Mech. Res. Commun.* **2010**, *37*, 47–49. [CrossRef]
24. Khojastehpour, M. Blunt crack-tip elastoplastic zone of mixed mode fracture. *Acta Mech. Solid. Sin.* **2014**, *27*, 531–541. [CrossRef]
25. Zhao, K.; Stead, D.; Kang, H.; Gao, F.; Donati, D. Three-dimensional simulation of hydraulic fracture propagation height in layered formations. *Environ. Earth Sci.* **2021**, *80*, 435. [CrossRef]
26. Wang, Y.; Chen, W. The shape function method of nonlinear thermal stress of granite fracture tips in a high-temperature environment. *Sci. Rep.* **2024**, *14*, 2736. [CrossRef] [PubMed]
27. Carslaw, H.S.; Jaeger, J.C. *Conduction of Heat in Solids*; Clarendon Press: Oxford, UK, 1959.
28. Li, M. Thermal–Moisture Stress Analysis of Tunnel Portal Rock in High Temperature and Humidity. Ph.D. Dissertation, Beijing Jiaotong University, Beijing, China, 2016. (In Chinese).
29. Wang, Y.; Shao, M.; Zhang, J.; Li, L.; Wang, N. Quantitative evaluation of alteration and exfoliation in Jurassic sandstone, Chongqing Danzishi rock carvings, China. *Eng. Geol.* **2021**, *292*, 106277. [CrossRef]

Disclaimer/Publisher's Note: The statements, opinions and data contained in all publications are solely those of the individual author(s) and contributor(s) and not of MDPI and/or the editor(s). MDPI and/or the editor(s) disclaim responsibility for any injury to people or property resulting from any ideas, methods, instructions or products referred to in the content.